materials

MDPI

Article

Microstructure Characteristics and Hydrogen Storage Kinetics of $Mg_{77+x}Ni_{20-x}La_3$ (x = 0, 5, 10, 15) Alloys

Hongxiao Tian [1], Qichang Wang [1], Xia Li [1], Long Luo [1] and Yongzhi Li [1,2,*]

[1] School of Science, Inner Mongolia University of Science and Technology, Baotou 014010, China; tianhongxiao@imust.edu.cn (H.T.)
[2] Baotou Materials Research Institute of Shanghai Jiao Tong University, Baotou 014010, China
* Correspondence: liyzh1983@imust.edu.cn

Abstract: $Mg_{77+x}Ni_{20-x}La_3$ (x = 0, 5, 10, 15) alloys were successfully prepared by the vacuum induction melting method. The structural characterizations of the alloys were performed by using X-ray diffraction and scanning electron microscope. The effects of nickel content on the microstructure and hydrogen storage kinetic of the as-cast alloys were investigated. The results showed that the alloys are composed of a primary phase of Mg_2Ni, lamella eutectic composites of Mg + Mg_2Ni, and some amount of $LaMg_{12}$ and La_2Mg_{17}. Nickel addition significantly improved the hydrogen-absorption kinetic performance of the alloy. At 683 K, $Mg_{77}Ni_{20}La_3$ alloy and $Mg_{82}Ni_{15}La_3$ alloy underwent hydrogen absorption and desorption reactions for 2 h, respectively, and their hydrogen absorption and desorption capacities were 4.16 wt.% and 4.1 wt.%, and 4.92 wt.% and 4.69 wt.%, respectively. Using the Kissinger equation, it was calculated that the activation energy values of $Mg_{77}Ni_{20}La_3$, $Mg_{82}Ni_{15}La_3$, $Mg_{87}Ni_{10}La_3$ and $Mg_{92}Ni_5La_3$ alloys were in the range of 68.5~75.2 kJ/mol, much lower than 150~160 kJ/mol of MgH_2.

Keywords: Mg-based alloy; lanthanum; microstructure; hydrogen storage kinetic

check for updates

Citation: Tian, H.; Wang, Q.; Li, X.; Luo, L.; Li, Y. Microstructure Characteristics and Hydrogen Storage Kinetics of $Mg_{77+x}Ni_{20-x}La_3$ (x = 0, 5, 10, 15) Alloys. *Materials* **2023**, *16*, 4576. https://doi.org/10.3390/ma16134576

Academic Editors: Jacques Huot, Giovanni Capurso and Fusheng Yang

Received: 22 May 2023
Revised: 14 June 2023
Accepted: 19 June 2023
Published: 25 June 2023

1. Introduction

Fossil fuels, the main energy source for the past two centuries, have caused energy crisis and environmental pollution problems due to excessive consumption [1–3]. Therefore, finding new energy sources is urgent [4]. Hydrogen is a clean energy source with many advantages such as versatility, high utilization efficiency, environmental compatibility, and inexhaustible [5]. Hydrogen energy economy involves hydrogen production, storage, transportation and application. Among them, hydrogen storage and transportation are the core and bottleneck technologies [6]. To achieve large-scale applications, the hydrogen storage system needs to be safe, efficient, and cost-effective [7]. Traditional gas storage, which can be pressurized up to 70 MPa with technical progress, pose considerable safety risk for mobile use [8]. Cryogenic liquid hydrogen storage, which consume more than 30% calorific value of the liquid hydrogen, are not suitable for popularization in the civil field [9]. Solid-state hydrogen storage materials are the first choice for large-scale hydrogen storage systems because of their safety, high capacity, and low pressure [10–13]. Magnesium-based alloys are the most viable solid-state hydrogen storage materials, owning to their low cost, high hydrogen storage capacity, high cycling stability and high safety [14–17]. However, the slow kinetics and high thermodynamics hinder their development [18].

A great deal of experimental researchers have been conducted in the last few decades to address the drawback of Mg-based alloys, such as alloying [19–21], nano-crystallization [22–24], doping catalyst [25–27] and exploring new treatment methods [28–30], etc. By alloying various transition metals (TM) with Mg, TM was found to reduce the thermal stability of MgH_2 and enhance the hydrogen reaction kinetics of MgH_2 [31,32]. Mg-Si alloys formed by alloying Mg and Si elements [33] can significantly reduce the thermal stability of the alloy. When Mg is alloyed with Ni elements, the hydrogen absorption/desorption phases transform from Mg/MgH_2 to Mg_2Ni/Mg_2NiH_4, and the dehydrogenation enthalpy decreases from 76 kJ/mol H_2 to 64 kJ/mol H_2 [34–36]. Ding et al. reported that the Mg-Mg_2Ni eutectic with a large amount of phase/grain boundaries is beneficial for the dissociation of H_2 and permeation of hydrogen atoms [34]. In addition, the enthalpy of hydrogen desorption of the Mg-In alloy [37] is reduced to 67.8 kJ/mol, which is very close to the Mg_2Ni system. The TM elements can be used as a special catalyst to lower the energy barrier for the recombination of hydrogen atoms and the decomposition of hydrogen molecules [38]. However, the Mg-TM alloys possess better hydrogen absorption/desorption kinetics with the expense of reversible hydrogen storage capacity [39,40].

Beside of TM, rare earth (RE) metals were also used widely for producing Mg-based alloys to enhance the hydrogenation kinetics. The in situ formed nano-scale rare earth hydrides (REH_x) bring interfacial channels and therefore facilitates the diffusion of hydrogen in the alloy [41–43]. Moreover, REH_x has a unique "hydrogen pumping" function, which can effectively reduce the apparent activation energy [44–46]. According to the Mg-La phase diagram [47], it is known that Mg-$LaMg_x$ eutectic can be formed even at very high Mg content. Lass et al. [48] found that after alloying with La, the reaction enthalpy of MgH_2 and Mg_2NiH_4 in the Mg-Ni alloy were reduced by 8 kJ/mol and 5 kJ/mol, respectively. REH_x in Mg-RE-TM alloys, which can be uniformly dispersed at the grain boundaries of the Mg matrix, effectively reduces the catalytic dead zone and improves the catalytic efficiency [49]. In addition, the stability of the nano phase structure of Mg-based alloys can be improved by pinning of REH_x to the Mg nano grain boundaries, which inhibits the growth of Mg/MgH_2 grains [50].

The balance between improving of reaction kinetics and decreasing of hydrogen storage capacity should be investigated carefully when increasing the proportion of Ni or RE in Mg-Ni-RE alloys. In the present study, $Mg_{77+x}Ni_{20-x}La_3$ (x = 0, 5, 10, 15) alloys were prepared by induction melting method. The microstructure, phase transformation and hydrogen storage kinetic of the alloys with different Mg and Ni ratios are studied. The synergistic catalytic effect of $LaH_{3.05}$ phase and Mg_2Ni phase on the hydrogen absorption and desorption process of the alloy was analyzed.

2. Materials and Methods

2.1. Material Preparation Methods

Alloys with the nominal composition of $Mg_{77+x}Ni_{20-x}La_3$ (x = 0, 5, 10, 15) were made from the appropriate amounts of pure magnesium, nickel, and lanthanum by using vacuum induction melting. The purity of the starting materials was not less than 99.5%, and the overall weight of the alloy was ~5 kg. Pure argon was used to fill in the furnace to prevent oxidation. The metallic solution was poured into an iron mold and cooled to indoor temperature. Afterward, the alloy ingots were mechanically pulverized into powder samples with a particle size of <200 mesh.

2.2. Structural Characterizations

The physical composition of the alloy was analysed by X-ray powder diffraction (XRD). The test instrument was a PANalytical X'pert Powder X-ray diffractometer from Panacor, Eindhoven, The Netherlands, using a Cu Kα target, a tube voltage of 40 kV, a current of 150 mA, sampling in a continuous scan mode, a scan speed of 2°/min, a step size of 0.02° and a scan range of 10–80°. To determine the phase composition of the alloy, XRD patterns were analysed using X'Pert HighScore Plus software, V3.8. After the ingot sections had been ground and polished in alcohol, the morphological structure of the ingot sections was observed using a TESCAN GAIA-3 (Tescan, Brno, Czech Republic) field emission scanning electron microscope (SEM) and the phase composition of the different morphological microzones was analysed using the energy spectrum analysis (EDS) supplied with the equipment. The block and powdered samples are glued to the metal base with conductive adhesive and the SEM is performed on the block before hydrogen absorption.

2.3. Hydrogen Storage Measurements

Hydrogen sorption kinetic tests were performed in a Sievert's apparatus under high-purity hydrogen (99.999% purity). Each sample weighed ~200 mg. The reactor was heated by a resistance furnace with an accuracy of ±0.5 K. Before measuring the hydrogenation kinetics, the samples were activated to three hydrogen absorption and desorption cycles at 653 K. Isothermal hydrogen absorption kinetic measurements were made in the temperature range from 473 to 683 K and with 3 MPa of hydrogen pressure. Calorimetric measurements of the full hydrogenated samples were also made using a NETZSCH (Selb, Germany) DSC 204 HP differential scanning calorimeter (DSC). The samples were heated from indoor temperature to 750 K with a heating rate of 5, 10, 20 and 40 K/min. The tests were performed under a pure argon flow (50 mL/min).

3. Results

3.1. Microstructure Characteristics

The X-ray diffraction patterns (XRD) of $Mg_{77+x}Ni_{20-x}La_3$ (x = 0, 5, 10, 15) alloys with four different Mg and Ni contents (x = 0, 5, 10, 15) are shown in Figure 1. The alloys before hydrogenation mainly consist of four phases: $LaMg_{12}$, Mg_2Ni, La_2Mg_{17} and Mg. As the Mg content increases, the intensities of $LaMg_{12}$, Mg_2Ni and La_2Mg_{17} phases gradually decrease for $Mg_{82}Ni_{15}La_3$ alloy. It is speculated that this is because the Mg content in the Mg phase increases, while the Mg content in the $LaMg_{12}$, Mg_2Ni and La_2Mg_{17} phases decreases accordingly. Therefore, the intensities of the diffraction peaks of $LaMg_{12}$, Mg_2Ni and La_2Mg_{17} phases decrease gradually. The grain boundaries formed between the multi-phase structures can provide channels for the diffusion of hydrogen sites and hydrogen atoms in the alloy. The defects and dislocations on the grain boundaries can lower the diffusion energy barrier of hydrogen atoms and enhance the diffusion coefficient of hydrogen atoms, thus accelerating the migration of hydrogen atoms in the alloy, which is conducive to improving the kinetic properties of the hydrogen absorption and desorption processes in the alloy. The C peak in the alloy is caused by the graphite crucible used to prepare the alloy in our experiment. The graphite crucible reacts with some metals at high temperatures to produce carbides, which are transferred to the alloy, resulting in the C-peak.

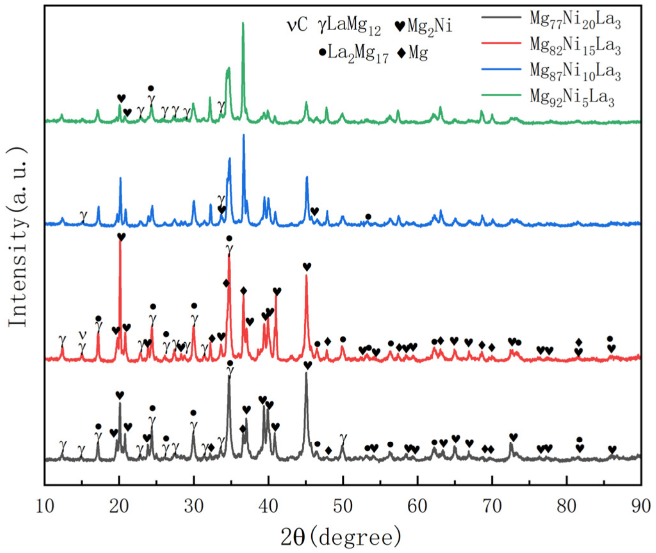

Figure 1. XRD patterns of the as-cast $Mg_{77+x}Ni_{20-x}La_3$ (x = 0, 5, 10, 15) alloys.

Figure 2 shows the XRD patterns of $Mg_{77+x}Ni_{20-x}La_3$ (x = 0, 5, 10, 15) alloys after saturated hydrogenation. It can be seen from the figure that the main phases of $Mg_{77}Ni_{20}La_3$ alloy after saturated hydrogenation are Mg_2NiH_4, MgH_2 and $LaH_{3.05}$, which are manifested as peaks with different positions and intensities on the XRD pattern. As the Mg content increases and the Ni content decreases, the intensity of the Mg_2NiH_4 phase diffraction peak gradually decreases, while the intensities of the MgH_2 and $LaH_{3.05}$ phase diffraction peaks increase significantly. This indicates that the La_2Mg_{17} and La_2Mg_{17} phases before hydrogenation of the alloy are completely transformed into $LaH_{3.05}$ and MgH_2 phases, and no unmelted Mg and Ni elements are generated.

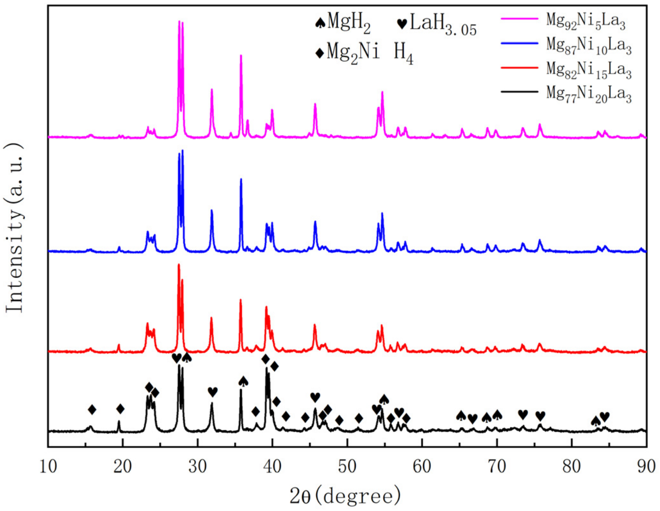

Figure 2. XRD patterns of the full hydrogenated $Mg_{77+x}Ni_{20-x}La_3$ (x = 0, 5, 10, 15) alloys.

Figure 3 shows the scanning electron microscope (SEM) images of the cross-sections of the $Mg_{77+x}Ni_{20-x}La_3$ (x = 0, 5, 10, 15) alloy ingots, showing the microstructure and phase composition of the alloys. As can be seen from the figure, the alloys are typical multiphase structures, represented by regions of different brightness. Combined with the EDS spectrum analysis of the corresponding regions in Figure 3a and the XRD test results, it can be known that the $Mg_{77}Ni_{20}La_3$ alloy mainly consists of four phases: Mg_2Ni, Mg, La_2Mg_{17} and $LaMg_{12}$, corresponding to the gray band-like regions, dark regions and bright continuous regions in the figure, respectively. The grey band in Figure 3a $Mg_{77}Ni_{20}La_3$ is determined to be the Mg_2Ni phase in combination with the phases identified by EDS spectroscopy and XRD in the corresponding region [51]. Similarly, the EDS energy spectrum analysis shows that the bright region is a coexistence of La_2Mg_{17} and $LaMg_{12}$ phases. In Figure 3b, $Mg_{82}Ni_{15}La_3$, the long band-like Mg_2Ni phase can be seen split into small pieces. The Mg phase gradually increases in the darker areas. The continuous bright areas begin to split into irregular polygons. Figure 3c The polygonal structure of the coexisting La_2Mg_{17} and $LaMg_{12}$ phases in the bright region of $Mg_{87}Ni_{10}La_3$ is more regular. Figure 3d The microstructure and structure of the alloy changes considerably with increasing Mg content in $Mg_{92}Ni_5La_3$. The grey and bright areas are uniformly distributed in the Mg matrix and show a typical eutectic structure consisting of Mg-Mg_2Ni, a layered structure of several hundred nanometers [52]. This layered eutectic structure provides an efficient channel for the diffusion of hydrogen atoms during the hydrogen absorption and release process of the alloy [53]. These changes are consistent with the above XRD analysis results.

The XRD and SEM results show that the alloy decomposes into $LaH_{3.05}$ and MgH_2 after reacting with H_2, which are formed from La_2Mg_{17} and $LaMg_{12}$ in the alloy. The XRD patterns of the hydrogenated alloy samples reveal that the diffraction peaks of the as-cast alloy phases disappear completely, and new peaks of metal hydrides emerge, including MgH_2, $LaH_{3.05}$ and Mg_2NiH_4. Thus, the first hydrogenation exothermic process of $Mg_{77+x}Ni_{20-x}La_3$ (x = 0, 5, 10, 15) alloy can be expressed by the following chemical equations:

$$Mg + H_2 \rightarrow MgH_2 \tag{1}$$

$$Mg_2Ni + H_2 \rightarrow Mg_2NiH_4 \tag{2}$$

$$LaMg_{12} + La_2Mg_{17} + H_2 \rightarrow LaH_{3.05} + MgH_2 \tag{3}$$

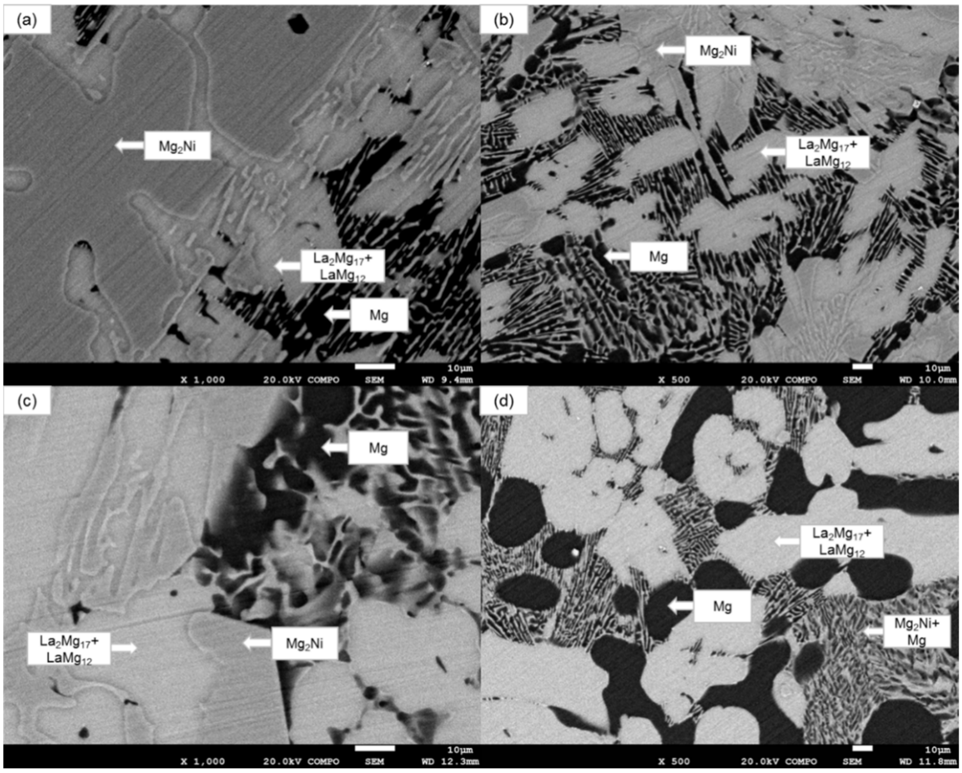

Figure 3. SEM images of the as-cast alloy ingots: (**a**) $Mg_{77}Ni_{20}La_3$; (**b**) $Mg_{82}Ni_{15}La_3$; (**c**) $Mg_{87}Ni_{10}La_3$, (**d**) $Mg_{92}Ni_5La_3$.

Moreover, after the dehydrogenation endothermic process, the MgH_2 phase is completely transformed into Mg phase, but the rare earth hydride phase ($LaH_{3.05}$) remains. This is because this kind of rare earth hydride has a high thermal stability [47], which cannot decompose under the current experimental conditions. Therefore, the reversible hydrogen absorption and desorption process of $Mg_{77+x}Ni_{20-x}La_3$ (x = 0, 5, 10, 15) alloy after activation can be represented by the following two chemical equations:

$$MgH_2 \leftrightarrow Mg + H_2 \tag{4}$$

$$Mg_2NiH_4 \leftrightarrow Mg_2Ni + H_2 \tag{5}$$

The stable $LaH_{3.05}$ nanocrystals uniformly distributed on the surface and bulk of the alloy during hydrogen absorption and desorption create a large number of boundaries and active sites for hydrogen atom diffusion. This not only facilitates the nucleation of Mg/MgH_2 and Mg_2Ni/Mg_2NiH_4, but also enhances the diffusion rate of hydrogen atoms in the alloy. Meanwhile, the existence of Mg-MgH_2 eutectic layered structure significantly increases the diffusion pathways of hydrogen atoms in the alloy. These two factors directly improve the kinetic properties of hydrogen absorption and desorption in the alloy.

3.2. Activation Behaviors and Hydrogen Absorption Kinetics

Figures 4 and 5 shows the activation curves of $Mg_{77+x}Ni_{20-x}La_3$ (x = 0, 5) alloy at 653 K. As shown in Figure 4a, the long-term hydrogen absorption curve of $Mg_{77}Ni_{20}La_3$ alloy indicates that the alloy has an initial activation hydrogen absorption of 4.67 wt.%, which is much higher than the second and third activation hydrogen absorptions. In Figure 4b, the long-term hydrogen absorption curve of $Mg_{82}Ni_{15}La_3$ alloy reveals that the alloy has an initial activation hydrogen absorption of 5.37 wt.%, while the second and third activation hydrogen absorptions are 5.16 wt.%, and the two curves almost overlap. This suggests that complete activation of the $Mg_{77}Ni_{20}La_3$ alloy at 653 K requires 3 hydrogenation cycles, while the $Mg_{82}N_{15}La_3$ alloy requires 2 hydrogenation cycles. In Figure 5a,b, the short-term hydrogen absorption curves of $Mg_{77}Ni_{20}La_3$ and $Mg_{82}Ni_{15}La_3$ alloys demonstrate that $Mg_{77}Ni_{20}La_3$ alloy takes much less time than $Mg_{82}Ni_{15}La_3$ alloy to reach the saturated hydrogen absorption (90%) in the second and third activations. This implies that $Mg_{77}Ni_{20}La_3$ alloy has a better activation performance than $Mg_{82}Ni_{15}La_3$ alloy. Moreover, it can also be seen from the short-term activation curves that the initial activation of the alloy is very slow.

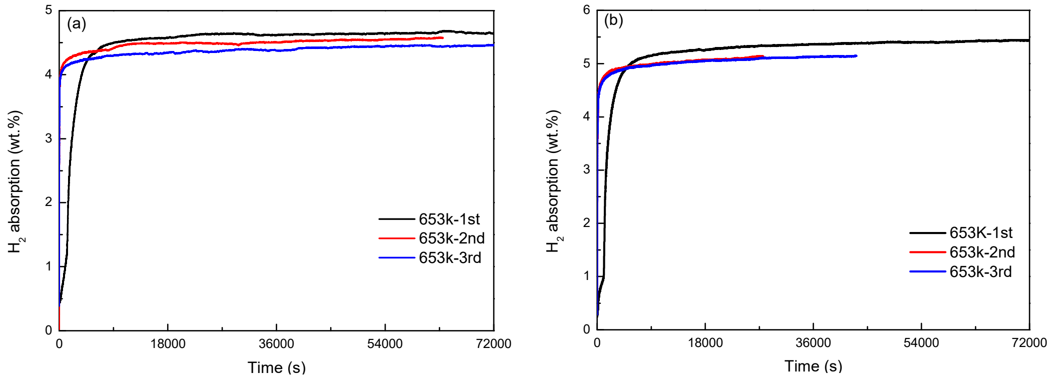

Figure 4. Long-time activation curves of $Mg_{77+x}Ni_{20-x}La_3$ ($x = 0, 5$) alloys at 653 K: (**a**) long-time hydrogen absorption by $Mg_{77}Ni_{20}La_3$; (**b**) long-time hydrogen absorption by $Mg_{82}Ni_{15}La_3$.

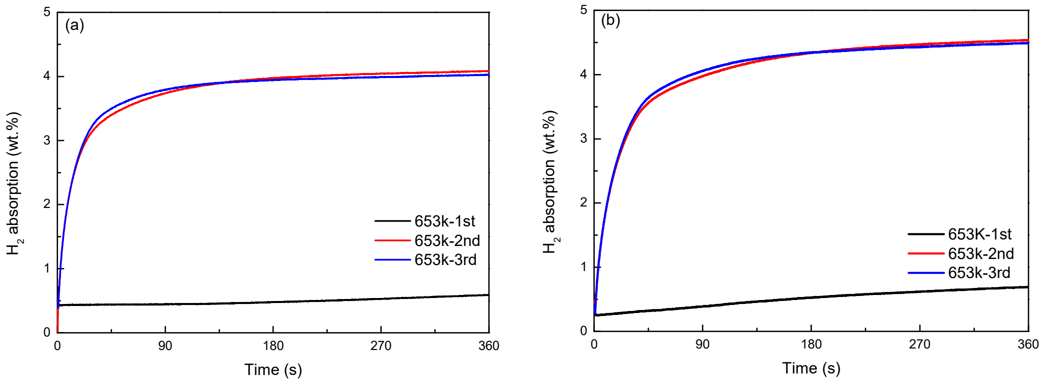

Figure 5. Short-time activation curves of $Mg_{77+x}Ni_{20-x}La_3$ ($x = 0, 5$) alloys at 653 K: (**a**) short-time hydrogen absorption by $Mg_{77}Ni_{20}La_3$; (**b**) short-time hydrogen absorption by $Mg_{82}Ni_{15}La_3$.

Figure 6 shows the hydrogen absorption kinetics curves of $Mg_{77+x}Ni_{20-x}La_3$ ($x = 0, 5$) alloy at different temperatures. As shown in Figure 6a, the hydrogen absorption of $Mg_{77}Ni_{20}La_3$ alloy reaches 4.02 wt.% at 533 K for 2 h, and the hydrogen absorption kinetics curves of $Mg_{77}Ni_{20}La_3$ alloy are almost identical when the temperature is above 533 K, indicating excellent hydrogen absorption kinetics properties. The hydrogen absorption at 623 K and 683 K are 4.3 wt.% and 4.16 wt.%, respectively. Figure 6b reveals that the hydrogen absorption of $Mg_{82}Ni_{15}La_3$ alloy attains as high as 4.92 wt.% at 683 K for 2 h. This is because the higher the Mg content, the stronger the hydrogen absorption ability of the alloy. The hydrogen absorption amount of the initial activation curve in $Mg_{77}Ni_{20}La_3$ and $Mg_{82}Ni_{15}La_3$ alloys is significantly higher than that of the alloy at each temperature, which is due to the formation of $LaH_{3.05}$ phase with high thermal stability and difficult to decompose after the initial hydrogenation of the alloy. In summary, $Mg_{82}Ni_{15}La_3$ alloy has better hydrogen absorption kinetics performance than $Mg_{77}Ni_{20}La_3$ alloy.

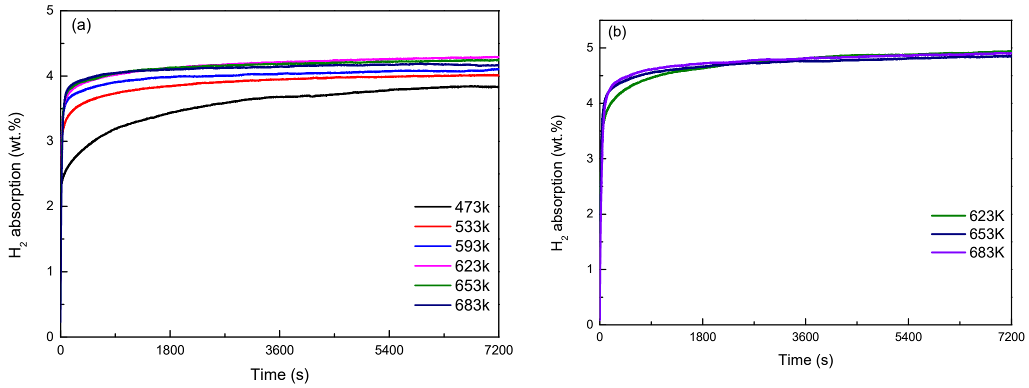

Figure 6. Hydrogen absorption kinetic curves of $Mg_{77+x}Ni_{20-x}La_3$ (x = 0, 5) alloys at various temperatures: (**a**) $Mg_{77}Ni_{20}La_3$; (**b**) $Mg_{82}Ni_{15}La_3$.

3.3. Hydrogen Desorption Kinetics and Activation Energy

Figures 7 and 8 show the hydrogen desorption endothermic reaction kinetics curves of $Mg_{77+x}Ni_{20-x}La_3$ (x = 0, 5) alloys at different temperatures. It can be seen from Figure 7a that $Mg_{77}Ni_{20}La_3$ alloy has the best hydrogen desorption working temperature above 623 K and reaches a hydrogen desorption amount of 4.1 wt.% at 683 K. It can be seen from Figure 7b that $Mg_{82}Ni_{15}La_3$ alloy has a hydrogen desorption amount of up to 4.69 wt.% at 683 K. This is because the higher the Mg content, the stronger the hydrogen desorption ability of the alloy. It can be seen from Figure 8a that the short-term hydrogen desorption endothermic kinetics curve of $Mg_{77}Ni_{20}La_3$ alloy shows that the maximum hydrogen desorption amount of the alloy is 3.8 wt.% at 653 K and reaches the saturated hydrogen desorption amount within 125 s. As the temperature increases, it only takes 71 s to reach a maximum hydrogen desorption amount of 3.8 wt.% at 683 K. This is mainly due to the increase of temperature, which increases the energy of reactants in the alloy, accelerates the hydrogen desorption rate of the alloy, and thus increases the hydrogen desorption amount. At the same time, Figure 8b shows that the short-term hydrogen desorption exothermic kinetics curve of $Mg_{82}Ni_{15}La_3$ alloy shows that the alloy reaches a saturated hydrogen desorption amount of 4.39 wt.% within 140 s at 653 K. And when the temperature rises to 683 K, $Mg_{82}Ni_{15}La_3$ alloy reaches a hydrogen desorption amount of 3.8 wt.% within 47 s.

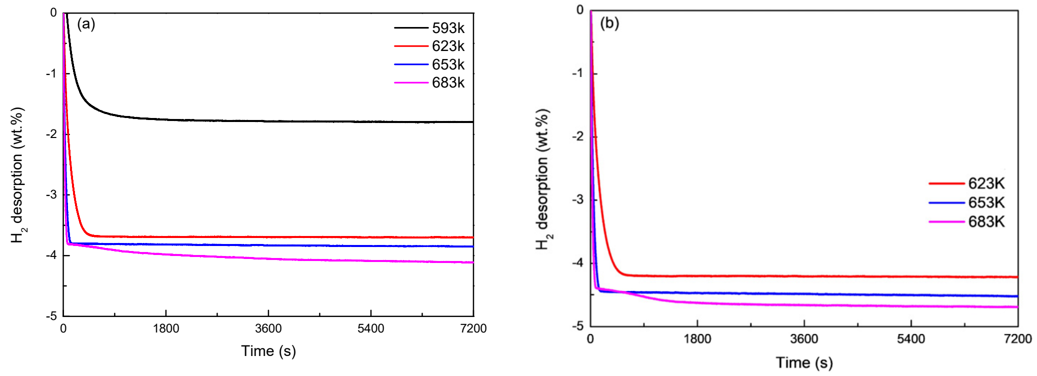

Figure 7. Long-time hydrogen desorption kinetic curves of $Mg_{77+x}Ni_{20-x}La_3$ (x = 0, 5) alloys at 653 K: (**a**) long-time hydrogen desorption by $Mg_{77}Ni_{20}La_3$; (**b**) long-time hydrogen desorption by $Mg_{82}Ni_{15}La_3$.

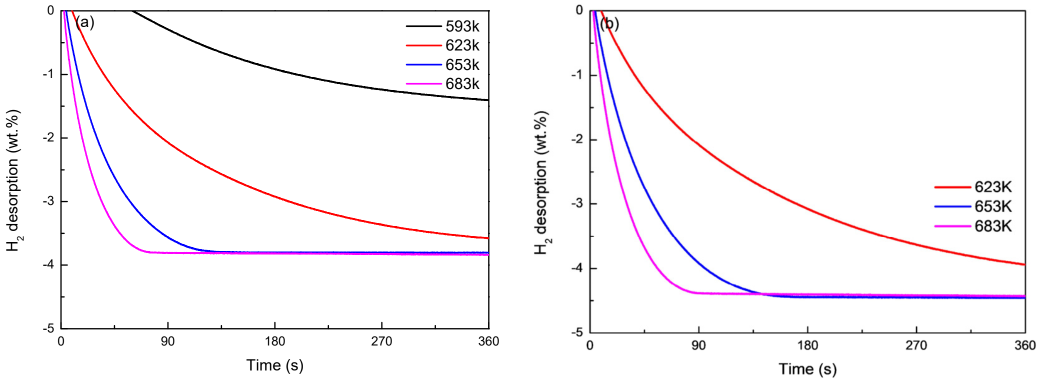

Figure 8. Short-time hydrogen desorption kinetic curves of $Mg_{77+x}Ni_{20-x}La_3$ (x = 0, 5) alloys at 653 K: (**a**) short-time hydrogen desorption by $Mg_{77}Ni_{20}La_3$; (**b**) short-time hydrogen desorption by $Mg_{82}Ni_{15}La_3$.

The phase change heat of the alloy was calculated by using the test method of the DSC curve of the alloy hydride warming and exothermic reaction. In order to calculate the phase transition heat of the alloy, we adopted the method of testing the DSC curve of the hydrogen desorption endothermic of the alloy hydride. Figure 9 shows the DSC curves of $Mg_{77+x}Ni_{20-x}La_3$ (x = 0, 5, 10, 15) alloy hydrides after saturated hydrogen absorption at different heating rates. The test temperature range was 400~700 K. Firstly, the initial temperature of the hydrogen desorption endothermic reaction of the alloy can be obtained from the DSC curve, and the activation energy of the hydrogen desorption endothermic reaction can be calculated according to the Kissinger method, so as to judge the difficulty of the reaction. It can be seen from Figure 9 that there is a clear exothermic main peak and a smaller peak on each DSC curve at each heating rate. The smaller exothermic peak is related to the phase transition of Mg_2NiH_4, by the coupled hydrogen desorption endothermic of MgH_2 and Mg_2NiH_4 phases. The temperature range of the smaller exothermic peak is between 513–522 K. In Figure 9a, the endothermic main peak consists of two obvious peaks, which confirms that the exothermic main peak is caused by two hydrogen desorption phases of MgH_2 and Mg_2NiH_4, while in Figure 9b–d, the exothermic main peak becomes an obvious peak, because two kinds of hydrogen desorption phases have a synergistic hydrogen desorption endothermic phenomenon. In Figure 9e, the exothermic peak temperature at 20 K/min heating rate shows that the phase transition peak temperature of Mg_2NiH_4 is little affected by Mg content and remains around 520 K. While the peak temperature of MgH_2 is more affected by Mg content and shows a trend of first rising and then falling. The increase of hydrogen desorption peak temperature causes the increase of activation energy of hydrogen desorption endothermic reaction of alloy hydride, which will be calculated in detail below. By comparing the hydrogen desorption endothermic temperatures corresponding to the exothermic main peaks of four alloys with different Mg contents at the same rate, it is found that with the increase of Mg content, the hydrogen desorption peak temperature of the alloy gradually increases and then decreases. $Mg_{87}Ni_{10}La_3$ alloy has the highest hydrogen desorption peak temperature at 20 K/min heating rate, which is 629.8 K; while $Mg_{92}Ni_5La_3$ alloy is 624.1 K, which is 5.7 K lower.

Table 1 lists the peak temperatures of DSC endothermic dehydrogenation reaction of $Mg_{77+x}Ni_{20-x}La_3$ (x = 0, 5, 10, 15) alloy hydrides at different heating rates. Using different heating rates and corresponding peak temperatures, the activation energy (Ea) of dehydrogenation endothermic reaction of the alloy can be calculated by Kissinger method.

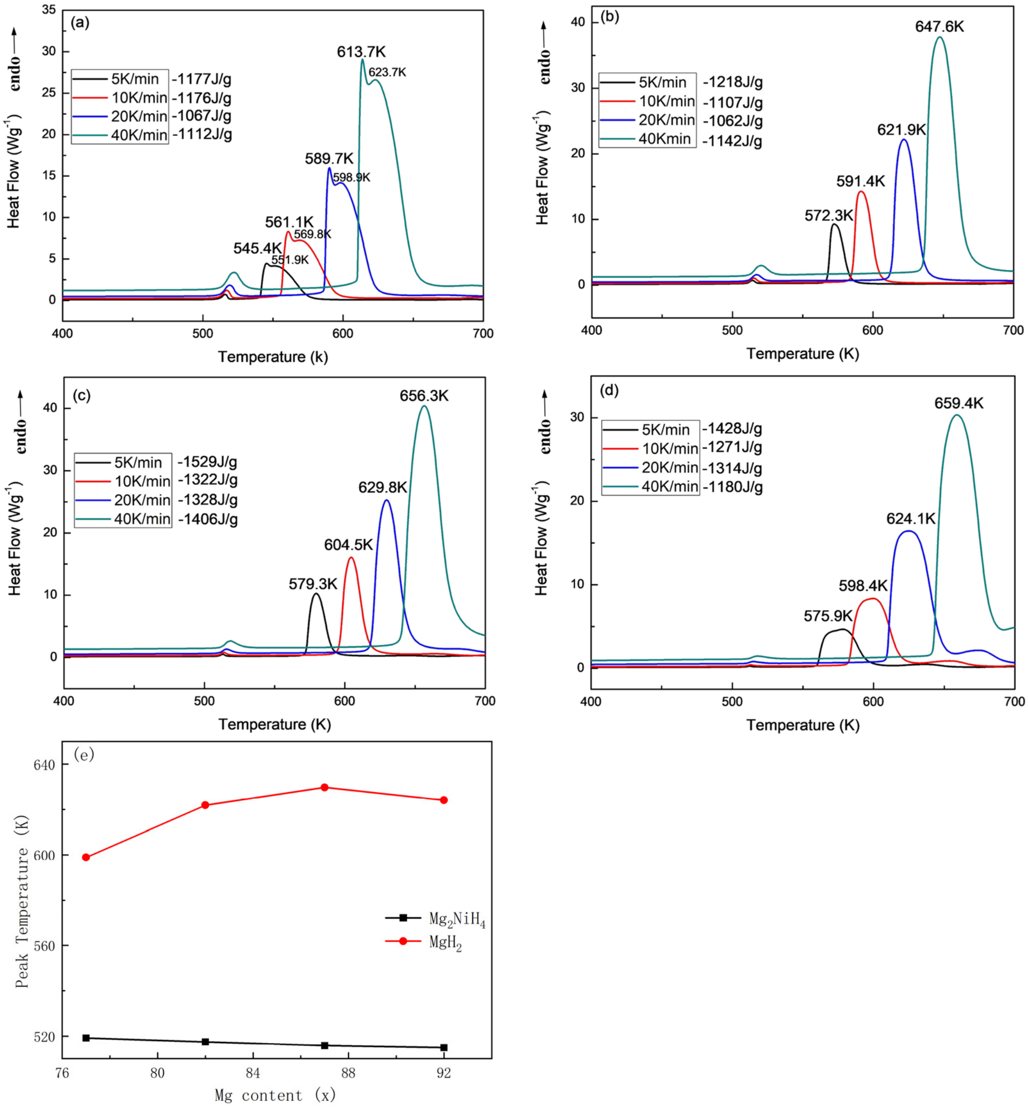

Figure 9. DSC curves of saturated hydrides of $Mg_{77+x}Ni_{20-x}La_3$ (x = 0, 5, 10, 15) alloys: (**a**) $Mg_{77}Ni_{20}La_3$; (**b**) $Mg_{82}Ni_{15}La_3$; (**c**) $Mg_{87}Ni_{10}La_3$; (**d**) $Mg_{92}Ni_5La_3$; (**e**) two peak heat absorption temperatures with increase of Mg content at 20 K/min heating rate contention.

Table 1. The peak temperature of $Mg_{77+x}Ni_{20-x}La_3$ (x = 0, 5, 10, 15) alloy hydrides during DSC dehydrogenation reaction at different heating rates.

Alloy	**5 K/min**		**10 K/min**		**20 K/min**		**40 K/min**	
	Mg_2NiH_4	**MgH_2**	**Mg_2NiH_4**	**MgH_2**	**Mg_2NiH_4**	**MgH_2**	**Mg_2NiH_4**	**MgH_2**
$Mg_{77}Ni_{20}La_3$	515.7	551.9	516.6	569.8	519.2	598.9	522.3	623.7
$Mg_{82}Ni_{15}La_3$	514.4	572.3	514.9	591.4	517.5	621.9	520.5	647.6
$Mg_{87}Ni_{10}La_3$	513.2	579.3	514.8	604.5	515.8	629.8	518.4	656.3
$Mg_{92}Ni_5La_3$	513.6	575.9	513.6	598.4	514.9	624.1	517.5	659.4

According to the Kissinger method, the activation energy can be calculated by using the following Equation (6):

$$\ln\left(\frac{\beta}{T_p^2}\right) = \frac{-E_a}{RT_P} + \ln(k_0) \tag{6}$$

where R is the gas constant, k_0 is a constant, T_p is the peak temperature of the exothermic peak, and β is the heating rate. This method was used to calculate the activation energy of $Mg_{77+x}Ni_{20-x}La_3$ (x = 0, 5, 10, 15) alloys at different heating rates.

Figure 10 shows the curve diagram after fitting according to the Kissinger equation. The fitting results show that the dehydrogenation activation energy of $Mg_{82}Ni_{15}La_3$ alloy is (72.7 ± 4.1) kJ/mol, the dehydrogenation activation energy of $Mg_{87}Ni_{10}La_3$ alloy is larger, which is (75.2 ± 1.5) kJ/mol, and the dehydrogenation activation energy of $Mg_{92}Ni_5La_3$ alloy is smaller, which is (68.5 ± 3.8) kJ/mol. Compared with $Mg_{87}Ni_{10}La_3$ alloy, the dehydrogenation endothermic activation energy of $Mg_{92}Ni_5La_3$ alloy is reduced by about 9%. Figure 10 shows that the activation energy values of $Mg_{77}Ni_{20}La_3$, $Mg_{82}Ni_{15}La_3$, $Mg_{87}Ni_{10}La_3$ and $Mg_{92}Ni_5La_3$ are between 68.5~75.2 kJ/mol. After comparison, these values are obviously lower than (150~160 kJ/mol) of MgH_2. The reason for the low activation energy value of the alloy is the effect of alloying and rare earth hydride formed by adding rare earth elements. In addition, due to the addition of rare earth element La to form rare earth hydride $LaH_{3.05}$ phase, and $LaH_{3.05}$ phase has "hydrogen pumping", which greatly reduces the hydrogen activation energy value of the alloy.

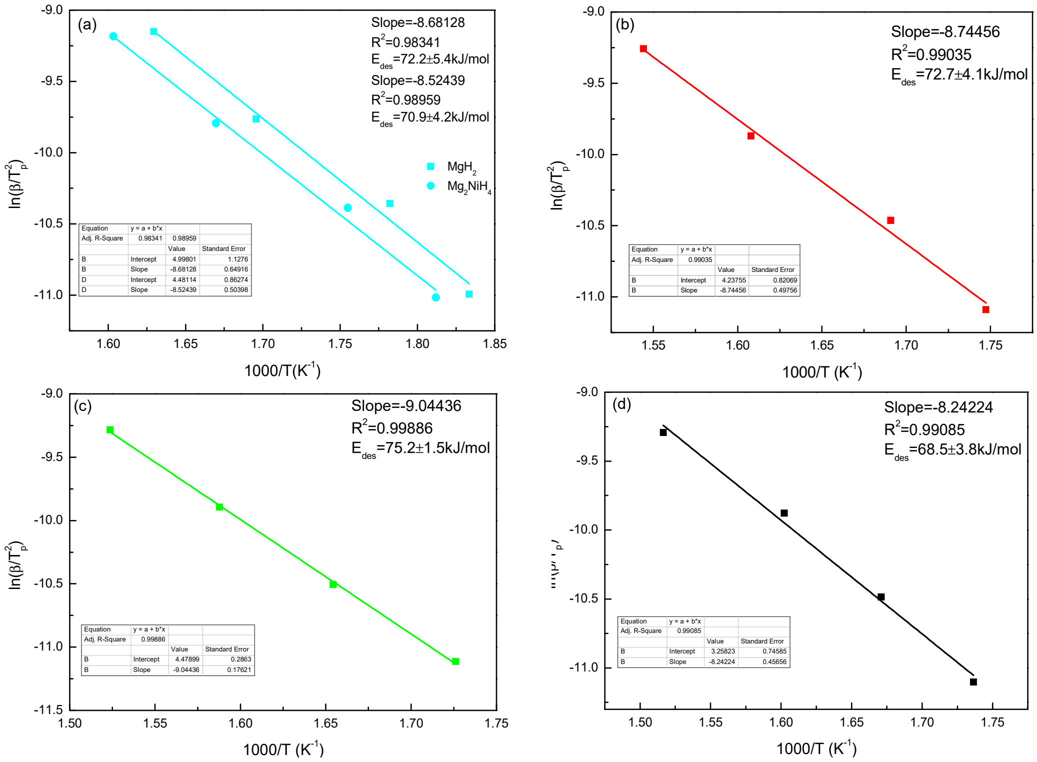

Equation	y = a + b*x		
Adj. R-Square	0.98341	0.98959	
		Value	Standard Error
B	Intercept	4.99801	1.1276
B	Slope	-8.68128	0.64916
D	Intercept	4.48114	0.86274
D	Slope	-8.52439	0.50398

Equation	y = a + b*x		
Adj. R-Square	0.99035		
		Value	Standard Error
B	Intercept	4.23755	0.82069
B	Slope	-8.74456	0.49756

Equation	y = a + b*x		
Adj. R-Square	0.99886		
		Value	Standard Error
B	Intercept	4.47899	0.2863
B	Slope	-9.04436	0.17621

Equation	y = a + b*x		
Adj. R-Square	0.99085		
		Value	Standard Error
B	Intercept	3.25823	0.74585
B	Slope	-8.24224	0.45656

Figure 10. Kissinger plot corresponding peak temperature of DSC at different heating rates of $Mg_{77+x}Ni_{20-x}La_3$ (x = 0, 5, 10, 15) alloys: (**a**) $Mg_{77}Ni_{20}La_3$; (**b**) $Mg_{82}Ni_{15}La_3$; (**c**) $Mg_{87}Ni_{10}La_3$; (**d**) $Mg_{92}Ni_5La_3$.

The increase of dehydrogenation temperature and dehydrogenation activation energy of alloy hydride is not conducive to the improvement of dehydrogenation kinetics performance of alloy. In $Mg_{77+x}Ni_{20-x}La_3$ (x = 0, 5, 10, 15) alloy, Mg content increases from Mg_{77} to Mg_{92}, and Ni content decreases from Ni_{20} to Ni_5. It can be seen from the hydrogen absorption and dehydrogenation kinetics curves of the alloy that the hydrogen absorption amount of the alloy shows an increasing trend. This is because after the increase of Mg content, the hydrogen absorption and desorption ability of Mg phase is higher than that of Mg_2Ni phase. And with the increase of hydrogen absorption and desorption cycle times, the hydrogen absorption and desorption ability of the alloy does not weaken obviously, and the alloy can achieve complete hydrogen absorption and desorption.

The peak temperature of hydrogen desorption endothermic reaction and phase transition heat for $Mg_{77+x}Ni_{20-x}La_3$ (x = 0, 5, 10, 15) alloy is presented in Table 2. The phase change heats are based on the DSC curves of the exothermic hydrides of the alloy after saturated hydrogen absorption at 5, 10, 20 and 40 K/min heating rates, calculated by the phase change heat (area of the peak) calculation function that comes with the DSC software. From the table, it can be seen that the phase change heat of $Mg_{77}Ni_{20}La_3$ alloy is 1177 J/g at a heating and desorption hydrogen rate of 5 K/min; the phase change heat of $Mg_{87}Ni_{10}La_3$ alloy is 1529 J/g; the phase change heat of $Mg_{92}Ni_5La_3$ alloy is 1428 J/g, which is 251 J/g higher than that of $Mg_{77}Ni_{20}La_3$ alloy. The phase change heat of $Mg_{92}Ni_5La_3$ alloy is second only to $Mg_{87}Ni_{10}La_3$ alloy, while the peak hydrogen desorption temperature is significantly lower than that of $Mg_{87}Ni_{10}La_3$, which is more favorable to the hydrogen desorption and heat absorption reaction of the alloy, but due to the high Mg content, it will lead to the alloy not releasing hydrogen. It can be seen from the analysis that with the increase of Mg content, the peak endothermic temperature of the alloy gradually increases, and the corresponding phase transition heat also gradually increases. It can be seen that the phase transition heat of $Mg_{87}Ni_{10}La_3$ alloy is significantly higher than that of the first two alloys and slightly higher than that of $Mg_{92}Ni_5La_3$ alloy. At the same time, the higher the Mg content in the alloy, the more likely the alloy will not desorption hydrogen. In summary, $Mg_{87}Ni_{10}La_3$ alloy is more suitable as an energy storage material.

Table 2. The peak temperature of hydrogen desorption endothermic reaction and phase transition heat for $Mg_{77+x}Ni_{20-x}La_3$ (x = 0, 5, 10, 15) alloy.

Alloy	**Peak Temperature/°C**				**Melting Enthalpy/J·g^{-1}**			
	5 K/min	**10 K/min**	**20 K/min**	**40 K/min**	**5 K/min**	**10 K/min**	**20 K/min**	**40 K/min**
$Mg_{77}Ni_{20}La_3$	545.4	561.1	589.7	613.7	−1177	−1176	−1067	−1112
$Mg_{82}Ni_{15}La_3$	572.3	591.4	621.9	647.6	−1218	−1107	−1062	−1142
$Mg_{87}Ni_{10}La_3$	579.3	604.5	629.8	656.3	−1529	−1322	−1328	−1406
$Mg_{92}Ni_5La_3$	575.9	598.4	624.1	659.4	−1428	−1271	−1314	−1180

4. Conclusions

The $Mg_{77+x}Ni_{20-x}La_3$ (x = 0, 5, 10, 15) alloy prepared by induction melting method mainly consists of three main phases: Mg_2Ni, $LaMg_{12}$, La_2Mg_{12} and residual Mg phase. After saturated hydrogen absorption, Mg_2Ni phase transforms into MgH_2 and $LaH_{3.05}$ phase. With the increase of Mg content, the long strip-like Mg_2Ni phase gradually disappears and transforms into Mg-Mg_2Ni eutectic lamellar structure. $Mg_{77+x}Ni_{20-x}La_3$ (x = 0, 5, 10, 15) alloys can be fully activated after 3 hydrogenation cycles at 653 K. The hydrogen absorption capacity of $Mg_{77}Ni_{20}La_3$ and $Mg_{82}Ni_{15}La_3$ alloys at 683 K for 2h are 4.92 wt.% and 4.69 wt.%, respectively. The hydrogen desorption activation energy of $Mg_{77}Ni_{20}La_3$ alloy is (70.9 ± 4.2) kJ/mol, $Mg_{82}Ni_{15}La_3$ alloy is (72.7 ± 4.1) kJ/mol, $Mg_{87}Ni_{10}La_3$ alloy is (75.2 ± 1.5) kJ/mol, and $Mg_{92}Ni_5La_3$ alloy is (68.5 ± 3.8) kJ/mol. The DSC test results show that the phase transition heat of $Mg_{82}Ni_{15}La_3$ alloy reaches 1529 J/g, which is 352 J/g higher than that of $Mg_{77}Ni_{20}La_3$ alloy.

Author Contributions: Conceptualization, Y.L.; Investigation, H.T., X.L. and Y.L.; Resources, L.L.; Writing—original draft, Q.W.; Writing—review & editing, Y.L.; Funding acquisition, Y.L. All authors have read and agreed to the published version of the manuscript.

Funding: This work was financially supported by the National Natural Science Foundations of China (52261041) and the Natural Science Foundation of Inner Mongolia, China (2020LH01006, 2020LH05024 and 2022MS05011).

Institutional Review Board Statement: The study did not require ethical approval. The study did not involve the use of humans or animals. Therefore, ethical review and approval were not required for this study. As per the guidelines, we confirm that the study was conducted in accordance with the Declaration of Helsinki.

Informed Consent Statement: Not applicable.

Data Availability Statement: Due to privacy and ethical restrictions, the data supporting the reported results of this study are unavailable for sharing. We acknowledge the importance of data sharing and encourage researchers to comply with data availability policies.

Conflicts of Interest: The authors declare no conflict of interest.

References

1. Zou, C.; Zhao, Q.; Zhang, G.; Xiong, B. Energy revolution: From a fossil energy era to a new energy era. *Nat. Gas Ind. B* **2016**, *3*, 1–11. [CrossRef]
2. Attia, N.F.; Menemparabath, M.M.; Arepalli, S.; Geckeler, K.E. Inorganic nanotube composites based on polyaniline: Potential room-temperature hydrogen storage materials. *Int. J. Hydrogen Energy* **2013**, *38*, 9251–9262. [CrossRef]
3. Li, L.; Jiang, G.; Tian, H.; Wang, Y. Effect of the hierarchical Co@C nanoflowers on the hydrogen storage properties of MgH_2. *Int. J. Hydrogen Energy* **2017**, *42*, 28464–28472. [CrossRef]
4. Liu, C.; Li, F.; Ma, L.P.; Cheng, H.M. Advanced materials for energy storage. *Adv. Mater.* **2010**, *22*, E28–E62. [CrossRef] [PubMed]
5. Chen, X.; Zou, J.; Zeng, X.; Ding, W. Hydrogen storage properties of a Mg-La-Fe-H nano-composite prepared through reactive ball milling. *J. Alloys Compd.* **2017**, *701*, 208–214. [CrossRef]
6. Kojima, Y. Hydrogen storage materials for hydrogen and energy carriers. *Int. J. Hydrogen Energy* **2019**, *44*, 18179–18192. [CrossRef]
7. Rusman, N.A.A.; Dahari, M. A review on the current progress of metal hydrides material for solid-state hydrogen storage applications. *Int. J. Hydrogen Energy* **2016**, *41*, 12108–12126. [CrossRef]
8. Stern, A.G. A new sustainable hydrogen clean energy paradigm. *Int. J. Hydrogen Energy* **2018**, *43*, 4244–4255. [CrossRef]
9. Lototskyy, M.V.; Davids, M.W.; Tolj, I.; Klochko, Y.V.; Sekhar, B.S.; Chidziva, S.; Smith, F.; Swanepoel, D.; Pollet, B.G. Metal hydride systems for hydrogen storage and supply for stationary and automotive low temperature PEM fuel cell power modules. *Int. J. Hydrogen Energy* **2015**, *40*, 11491–11497. [CrossRef]
10. Gosalawit–Utke, R.; Thiangviriya, S.; Javadian, P.; Laipple, D.; Pistidda, C.; Bergemann, N.; Horstmann, C.; Jensen, T.R.; Klassen, T.; Dornheim, M. Effective nanoconfinement of $2LiBH_4$–MgH_2 via simply MgH_2 premilling for reversible hydrogen storages. *Int. J. Hydrogen Energy* **2014**, *39*, 15614–15626. [CrossRef]
11. Ali, N.A.; Idris, N.H.; Din, M.F.M.; Yahya, M.; Ismail, M. Nanoflakes $MgNiO_2$ synthesised via a simple hydrothermal method and its catalytic roles on the hydrogen sorption performance of MgH_2. *J. Alloys Compd.* **2019**, *796*, 279–286. [CrossRef]
12. Ren, J.; Musyoka, N.M.; Langmi, H.W.; Mathe, M.; Liao, S. Current research trends and perspectives on materials-based hydrogen storage solutions: A critical review. *Int. J. Hydrogen Energy* **2017**, *42*, 289–311. [CrossRef]
13. Wu, Z.; Zhu, L.; Yang, F.; Jiang, Z.; Zhang, Z. First-principles insights into influencing mechanisms of metalloid B on Mg-based hydrides. *J. Alloys Compd.* **2017**, *693*, 979–988. [CrossRef]
14. Ismail, M. Effect of adding different percentages of $HfCl_4$ on the hydrogen storage properties of MgH_2. *Int. J. Hydrogen Energy* **2021**, *46*, 8621–8628. [CrossRef]
15. Sakintuna, B.; Lamari-Darkrim, F.; Hirscher, M. Metal hydride materials for solid hydrogen storage: A review. *Int. J. Hydrogen Energy* **2007**, *32*, 1121–1140. [CrossRef]
16. Ren, S.; Fu, Y.; Zhang, L.; Cong, L.; Xie, Y.; Yu, H.; Wang, W.; Li, Y.; Jian, L.; Wang, Y.; et al. An improved hydrogen storage performance of MgH_2 enabled by core-shell structure Ni/Fe_3O_4@ MIL. *J. Alloys Compd.* **2022**, *892*, 162048. [CrossRef]
17. Jain, I.P.; Lal, C.; Jain, A. Hydrogen storage in Mg: A most promising material. *Int. J. Hydrogen Energy* **2010**, *35*, 5133–5144. [CrossRef]
18. Yartys, V.A.; Lototskyy, M.V.; Akiba, E.; Albert, R.; Antonov, V.; Ares, J.; Baricco, M.; Bourgeois, N.; Buckley, C.; von Colbe, J.B.; et al. Magnesium based materials for hydrogen based energy storage: Past; present and future. *Int. J. Hydrogen Energy* **2019**, *44*, 7809–7859. [CrossRef]
19. Kang, H.; Yong, H.; Wang, J.; Xu, S.; Li, L.; Wang, S.; Hu, J.; Zhang, Y. Characterization on the kinetics and thermodynamics of Mg-based hydrogen storage alloy by the multiple alloying of Ce; Ni and Y elements. *Mater. Charact.* **2021**, *182*, 111583. [CrossRef]
20. Zhang, H.; Fu, L.; Qi, J.; Ji, Z. Effects of doping with yttrium on the hydrogen storage performances of the La_2Mg_{17} alloy surface. *J. Power Sources* **2019**, *417*, 76–82. [CrossRef]
21. Akbarzadeh, F.Z.; Rajabi, M. Mechanical alloying fabrication of nickel/cerium/MgH_2 nanocomposite for hydrogen storage: Molecular dynamics study and experimental verification. *J. Alloys Compd.* **2022**, *899*, 163280. [CrossRef]
22. Yuan, Z.; Li, X.; Li, T.; Zhai, T.; Lin, Y.; Feng, D.; Zhang, Y. Improved hydrogen storage performances of nanocrystalline RE_5Mg_{41}-type alloy synthesized by ball milling. *J. Energy Storage* **2022**, *46*, 103702. [CrossRef]

23. Guo, F.; Zhang, T.; Shi, L.; Chen, Y.; Song, L. Mechanisms of hydrides' nucleation and the effect of hydrogen pressure induced driving force on hydrogen absorption/desorption kinetics of Mg-based nanocrystalline alloys. *Int. J. Hydrogen Energy* **2022**, *47*, 1063–1075. [CrossRef]
24. Li, Y.; Liu, Z.; Zhang, Y.; Ren, H. A comparative study on the microstructure and cycling stability of the amorphous and nanocrystallization $Mg_{60}Ni_{20}La_{10}$ alloys. *Int. J. Hydrogen Energy* **2018**, *43*, 19141–19151. [CrossRef]
25. Sazelee, N.; Md Din, M.F.; Ismail, M.; Rather, S.-U.; Bamufleh, H.S.; Alhumade, H.; Taimoor, A.A.; Saeed, U. Effect of $LaCoO_3$ synthesized via solid-state method on the hydrogen storage properties of MgH2. *Materials* **2023**, *16*, 2449. [CrossRef]
26. Yong, H.; Wei, X.; Wang, Y.; Guo, S.; Yuan, Z.; Qi, Y.; Zhao, D.; Zhang, Y. Phase evolution; thermodynamics and kinetics property of transition metal (TM = Zr; Ti; V) catalyzed Mg–Ce–Y–Ni hydrogen storage alloys. *J. Phys. Chem. Solids* **2020**, *144*, 109516. [CrossRef]
27. Suárez-Alcántara, K.; Flores-Jacobo, N.I.; Osorio-García, M.P.; Cabañas-Moreno, J.G. Fast Hydrogen Sorption Kinetics in Mg-VCl3 Produced by Cryogenic Ball-Milling. *Materials* **2023**, *16*, 2526. [CrossRef] [PubMed]
28. Chen, J.N.; Zhang, J.; He, J.H.; Zhou, X.; Lu, X.; Chen, X.; Yu, L.; Zhou, D. A comparative study on hydrogen storage properties of as-cast and extruded Mg-4.7 Y-4.1 Nd-0.5 Zr alloys. *J. Phys. Chem. Solids* **2022**, *161*, 110483. [CrossRef]
29. Lyu, J.; Elman, R.; Svyatkin, L.; Kudiiarov, V. Theoretical and Experimental Studies of Al-Impurity Effect on the Hydrogenation Behavior of Mg. *Materials* **2022**, *15*, 8126. [CrossRef]
30. Zhang, J.; Yao, Y.; He, L.; Zhou, X.; Yu, L.; Lu, X.; Peng, P. Hydrogen storage properties and mechanisms of as-cast; homogenized and ECAP processed $Mg_{98.5}Y_1Zn_{0.5}$ alloys containing LPSO phase. *Energy* **2021**, *217*, 119315. [CrossRef]
31. Pozzo, M.; Alfe, D. Hydrogen dissociation and diffusion on transition metal (= Ti; Zr; V.; Fe; Ru; Co; Rh; Ni; Pd; Cu; Ag)-doped Mg (0001) surfaces. *Int. J. Hydrogen Energy* **2009**, *34*, 1922–1930. [CrossRef]
32. Cui, J.; Liu, J.; Wang, H.; Ouyang, L.; Sun, D.; Zhu, M.; Yao, D. Mg–TM (TM: Ti; Nb; V.; Co; Mo or Ni) core–shell like nanostructures: Synthesis; hydrogen storage performance and catalytic mechanism. *J. Mater. Chem. A* **2014**, *2*, 9645–9655. [CrossRef]
33. Tan, Z.; Ouyang, L.; Liu, J.; Wang, H.; Shao, H.; Zhu, M. Hydrogen generation by hydrolysis of Mg-Mg_2Si composite and enhanced kinetics performance from introducing of $MgCl_2$ and Si. *Int. J. Hydrogen Energy* **2018**, *43*, 2903–2912. [CrossRef]
34. Ding, X.; Chen, R.; Jin, Y.; Chen, X.; Guo, J.; Su, Y.; Ding, H.; Fu, H. Activation mechanism and dehydrogenation behavior in bulk hypo/hyper-eutectic Mg-Ni alloy. *J. Power Sources* **2018**, *374*, 158–165. [CrossRef]
35. Khan, D.; Zou, J.; Zeng, X.; Ding, W. Hydrogen storage properties of nanocrystalline Mg_2Ni prepared from compressed $2MgH_2Ni$ powder. *Int. J. Hydrogen Energy* **2018**, *43*, 22391–22400. [CrossRef]
36. Čermák, J.; Král, L. Hydrogen diffusion in Mg–H and Mg–Ni–H alloys. *Acta Mater.* **2008**, *56*, 2677–2686. [CrossRef]
37. Zhou, C.; Fang, Z.Z.; Lu, J.; Zhang, X. Thermodynamic and kinetic destabilization of magnesium hydride using Mg–In solid solution alloys. *J. Am. Chem. Soc.* **2013**, *135*, 10982–10985. [CrossRef] [PubMed]
38. Korablov, D.; Besenbacher, F.; Jensen, T.R. Kinetics and thermodynamics of hydrogenation-dehydrogenation for Mg-25% TM (TM = Ti; Nb or V) composites synthesized by reactive ball milling in hydrogen. *Int. J. Hydrogen Energy* **2018**, *43*, 16804–16814. [CrossRef]
39. El-Eskandarany, M.S.; Shaban, E.; Ali, N.; Aldakheel, F.; Alkandary, A. In-situ catalyzation approach for enhancing the hydrogenation/dehydrogenation kinetics of MgH_2 powders with Ni particles. *Sci. Rep.* **2016**, *6*, 37335. [CrossRef]
40. Ouyang, L.Z.; Huang, J.M.; Wang, H.; Wen, Y.; Zhang, Q.; Sun, D.; Zhu, M. Excellent hydrolysis performances of Mg_3RE hydrides. *Int. J. Hydrogen Energy* **2013**, *38*, 2973–2978. [CrossRef]
41. Zhang, Q.A.; Liu, D.D.; Wang, Q.Q.; Fang, F.; Sun, D.; Ouyang, L.; Zhu, M. Superior hydrogen storage kinetics of $Mg_{12}YNi$ alloy with a long-period stacking ordered phase. *Scr. Mater.* **2011**, *65*, 233–236. [CrossRef]
42. Ouyang, L.Z.; Yang, X.S.; Zhu, M.; Li, J.; Dong, H.; Sun, D.; Zou, J.; Yao, X. Enhanced hydrogen storage kinetics and stability by synergistic effects of in situ formed $CeH_{2.73}$ and Ni in $CeH_{2.73}$-MgH_2-Ni nanocomposites. *J. Phys. Chem. C* **2014**, *118*, 7808–7820. [CrossRef]
43. Pang, X.; Ran, L.; Luo, Y.; Luo, Y.; Pan, F. Enhancing hydrogen storage performance via optimizing Y and Ni element in magnesium alloy. *J. Magnes. Alloys* **2022**, *10*, 821–835. [CrossRef]
44. Guo, F.; Zhang, T.; Shi, L.; Song, L. Composition dependent microstructure evolution; activation and hydrogen absorption/desorption properties of Mg–Ni–La alloys. *Int. J. Hydrogen Energy* **2019**, *44*, 16745–16756. [CrossRef]
45. Yong, H.; Guo, S.; Yuan, Z.; Qi, Y.; Zhao, D.; Zhang, Z. Catalytic effect of in situ formed Mg_2Ni and REH_x (RE: Ce and Y) on thermodynamics and kinetics of Mg-RE-Ni hydrogen storage alloy. *Renew. Energy* **2020**, *157*, 828–839. [CrossRef]
46. Kang, Y.B.; Jin, L.; Chartrand, P.; Gheribi, A.E.; Bai, K.; Wu, P. Thermodynamic evaluations and optimizations of binary Mg-light rare Earth (La; Ce; Pr; Nd; Sm) systems. *Calphad* **2012**, *38*, 100–116. [CrossRef]
47. Ding, X.; Chen, R.; Zhang, J.; Chen, X.; Su, Y.; Guo, J. Achieving superior hydrogen storage properties via in-situ formed nanostructures: A high-capacity Mg–Ni alloy with La microalloying. *Int. J. Hydrogen Energy* **2022**, *47*, 6755–6766. [CrossRef]
48. Lass, E.A. Hydrogen storage measurements in novel Mg-based nanostructured alloys produced via rapid solidification and devitrification. *Int. J. Hydrogen Energy* **2011**, *36*, 10787–10796. [CrossRef]
49. Zhang, J.; Ding, X.; Chen, R.; Cao, W.; Su, Y.; Guo, J. Design of LPSO-introduced $Mg_{96}Y_2Zn_2$ alloy and its improved hydrogen storage properties catalyzed by in-situ formed YH_2. *J. Alloys Compd.* **2022**, *910*, 164832. [CrossRef]

50. He, J.H.; Zhang, J.; Zhou, X.J.; Chen, J.; Yu, L.; Jiang, L.; Jiang, K.; Lu, X.; Chen, X.; Zhou, Z. Hydrogen storage properties of $Mg_{98.5}Gd_1Zn_{0.5}$ and $Mg_{98.5}Gd_{0.5}Y_{0.5}Zn_{0.5}$ alloys containing LPSO phases. *Int. J. Hydrogen Energy* **2021**, *46*, 32949–32961. [CrossRef]
51. Tanaka, K.; Kanda, Y.; Furuhashi, M.; Saito, K.; Kuroda, K.; Saka, H. Improvement of hydrogen storage properties of melt-spun Mg–Ni–RE alloys by nanocrystallization. *J. Alloys Compd.* **1999**, *293*, 521–525. [CrossRef]
52. Li, Y.; Yang, J.; Luo, L.; Hu, F.; Zhai, T.; Zhao, Z.; Zhang, Z.; Zhao, D. Microstructure characteristics, hydrogen storage kinetic and thermodynamic properties of $Mg_{80-x}Ni_{20}Y_x$ (x= 0 –7) alloys. *Int. J. Hydrogen Energy* **2019**, *44*, 7371–7380. [CrossRef]
53. Poletaev, A.A.; Denys, R.V.; Solberg, J.K.; Tarasov, B.P.; Yartys, V.A. Microstructural optimization of $LaMg_{12}$ alloy for hydrogen storage. *J. Alloys Compd.* **2011**, *509*, S633–S639. [CrossRef]